Single-frequency approximation of the coupling ray theory

Luděk Klimeš & Petr Bulant
Department of Geophysics, Faculty of Mathematics and Physics, Charles University, Ke Karlovu 3, 121 16 Praha 2, Czech Republic,
http://sw3d.cz/staff/klimes.htm, http://sw3d.cz/staff/bulant.htm

Summary

The coupling–ray–theory Green tensor is frequency dependent, and is usually calculated for many frequencies. This frequency dependence represents no problem for calculating the Green tensor, but may represent a great problem when storing the Green tensor at the nodes of dense grids, typical for applications such as seismic migrations. This paper is devoted to the approximation of the coupling–ray–theory Green tensor, which eliminates this frequency dependence.

In the vicinity of a given prevailing frequency, we approximate the frequency–domain coupling–ray–theory Green tensor by two Green tensors corresponding to two S waves described by their travel times and amplitudes. We refer to these travel times and amplitudes as the coupling–ray–theory travel times and the coupling–ray–theory amplitudes. This "single–frequency approximation" of the coupling ray theory allows us to process the coupling–ray–theory wavefield in the same way as the anisotropic–ray–theory wavefield. This simplification may be decisive when storing the Green tensor at the nodes of dense grids, which is typical for applications such as seismic migrations.

We test the accuracy of the proposed single–frequency approximation of the coupling ray theory numerically in eight anisotropic velocity models. The additional inaccuracy introduced by the single–frequency approximation is smaller than the inaccuracy of the standard frequency–domain coupling ray theory, and smaller than the additional inaccuracy introduced by many other approximations of the coupling ray theory.

Keywords

S–wave coupling, Green tensor, travel time, amplitude, anisotropy, heterogeneous media, wave propagation.

1. Introduction

There are two different high–frequency asymptotic ray theories with frequency–independent amplitudes: the *isotropic ray theory* based on the assumption of equal velocities of both S waves, and the *anisotropic ray theory* assuming both S waves strictly decoupled. Here the term "different" means that the isotropic ray theory is not a special case of the anisotropic ray theory for decreasing anisotropy, and that both theories yield different S waves in equal velocity models.

In the isotropic ray theory, the S–wave polarization vectors do not rotate about the ray, whereas in the anisotropic ray theory they coincide with the eigenvectors of the Christoffel matrix which may rotate rapidly about the ray. Thomson, Kendall & Guest (1992) demonstrated analytically that the high–frequency asymptotic error of the

In: Seismic Waves in Complex 3–D Structures, Report 22 (Department of Geophysics, Charles University, Prague, 2012), pp. 143–167

anisotropic–ray–theory wavefield is inversely proportional to the second or higher root of the frequency if a ray passes through the point of equal S–wave eigenvalues of the Christoffel matrix even in otherwise strongly anisotropic media.

In "weakly anisotropic" models, at moderate frequencies, the S–wave polarization tends to remain unrotated round the ray, but is partly attracted by the rotation of the eigenvectors of the Christoffel matrix. The intensity of the attraction increases with frequency. This behaviour of the S–wave polarization is described by the *coupling ray theory* proposed by Coates & Chapman (1990). The frequency–dependent coupling ray theory is the generalization of both the zero–order isotropic and anisotropic ray theories and provides continuous transition between them. The coupling ray theory is applicable to S waves at all degrees of anisotropy, from isotropic to considerably anisotropic velocity models. The numerical algorithm for calculating the frequency–dependent complex–valued S–wave polarization vectors of the coupling ray theory has been designed by Bulant & Klimeš (2002).

The coupling ray theory can be derived from the asymptotic ray series referred to as the coupling ray series (Klimeš, 2007). This derivation demonstrates that there are many possible forms of the coupling ray theory of varying accuracy, and that the currently used coupling ray theory proposed by Coates & Chapman (1990) need not represent the most accurate option. Moreover, there are many more or less accurate approximations of this coupling ray theory (Bulant & Klimeš, 2002; Pšenčík & Farra, 2005; 2007; Farra & Pšenčík, 2008; 2010). Note that the anisotropic–common–ray approximation (Klimeš, 2006; Klimeš & Bulant, 2006) usually preserves the accuracy of the coupling ray theory and simultaneously considerably simplifies ray tracing by eliminating S–wave slowness surface singularities.

The coupling–ray–theory Green tensor is frequency dependent, and is usually calculated for many frequencies. This frequency dependence represents no problem in calculating the Green tensor, but may represent a great problem when storing the Green tensor at the nodes of dense grids, typical for applications such as seismic migrations. This paper is devoted to the approximation of the coupling–ray–theory Green tensor, which eliminates this frequency dependence within a limited frequency band.

In the vicinity of a given prevailing frequency, we approximate the frequency–domain coupling–ray–theory Green tensor by two Green tensors corresponding to two S waves described by their travel times and amplitudes. We refer to these travel times and amplitudes as the coupling–ray–theory travel times and the coupling–ray–theory amplitudes. The presented numerical examples suggest that the coupling–ray–theory travel times are usually close to the anisotropic–ray–theory travel times. However, if the rays pass close to a conical or similar S–wave singularity, the singularity acts as an interface and approximately converts the S–wave polarizations from S1 to S2, and vice versa. In this case, the coupling–ray–theory travel times correspond approximately to the anisotropic–ray–theory travel times of the S1S2 and S2S1 waves converted at the S–wave singularity.

2. Coupling ray theory

2.1. Coupling equation

The coupling equation is solved along a *reference ray*, and thus slightly depends on the selection of the reference ray. The reference ray is usually represented by the ray calculated using a reference Hamiltonian function.

There are various more or less accurate forms of the *coupling equation*. We consider here the frequency–domain coupling equation (Bulant & Klimeš, 2002, eq. 11)

$$\mathbf{\Pi}' = \left[\begin{pmatrix} 0 & 1 \\ -1 & 0 \end{pmatrix} \varphi' - \begin{pmatrix} \mathrm{i} & 0 \\ 0 & -\mathrm{i} \end{pmatrix} \varepsilon' \right] \mathbf{\Pi} \tag{1}$$

for 2×2 propagator matrix $\mathbf{\Pi}$ with identity initial conditions. The resulting matrix $\mathbf{\Pi}$ is unitary and unimodular, $\mathbf{\Pi}^{-1} = \mathbf{\Pi}^{+}$ and $\det(\mathbf{\Pi}) = 1$, which directly follows from coupling equation (1). Note that there may exist more accurate forms of the coupling equation (Klimeš, 2007).

Here prime $'$ denotes the derivative along the reference ray, and

$$\varepsilon = \tfrac{1}{2}\,\omega\left(\tau^{(2)} - \tau^{(1)}\right) \quad , \tag{2}$$

where $\omega = 2\pi f$ is the circular frequency, and $\tau^{(1)}$ and $\tau^{(2)}$ are the anisotropic–ray–theory travel times corresponding to S–wave eigenvectors $g_i^{(1)}$ and $g_i^{(2)}$ of the Christoffel matrix, see Section 2.3. The accuracy of the coupling ray theory is affected considerably by the accuracy of the calculation of $\tau^{(1)}$, $\tau^{(2)}$, $g_i^{(1)}$ and $g_i^{(2)}$.

The angular velocity of rotation of the eigenvectors is characterized by quantity

$$\varphi' = \mathrm{sgn}(\varphi'_{(12)})\sqrt{|\varphi'_{(12)}\varphi'_{(21)}|} = -\mathrm{sgn}(\varphi'_{(21)})\sqrt{|\varphi'_{(12)}\varphi'_{(21)}|} \quad , \tag{3}$$

where

$$\varphi'_{(KL)} = -g_i^{(K)}\left(g_i^{(L)}\right)' \quad . \tag{4}$$

This definition of φ' is a generalization of the definition of Bulant & Klimeš (2002, eq. 5) to non–orthogonal vectors $g_i^{(1)}$ and $g_i^{(2)}$, see Klimeš (2007, eq. 45).

2.2. Coupling–ray–theory Green tensor

The frequency–domain coupling–ray–theory Green tensor then reads

$$G_{ij}(\mathbf{x},\mathbf{x}_0,\omega) = \sum_{K,L=1}^{2} A(\mathbf{x},\mathbf{x}_0)\; g_i^{(K)}(\mathbf{x})\, g_j^{(L)}(\mathbf{x}_0)\, \Pi_{KL}(\mathbf{x},\mathbf{x}_0,\omega) \exp[\mathrm{i}\omega\overline{\tau}(\mathbf{x},\mathbf{x}_0)] \quad , \tag{5}$$

where

$$\overline{\tau} = \tfrac{1}{2}\left(\tau^{(1)} + \tau^{(2)}\right) \quad , \tag{6}$$

and A is the reference amplitude which serves here as a substitute for the correct individual amplitudes. Reference amplitude A is usually calculated for the reference Hamiltonian function.

2.3. Reference and perturbation Hamiltonian functions

The reference ray for the coupling equation is calculated using the reference Hamiltonian function. We consider reference Hamiltonian function

$$H(x_m,p_n)=\tfrac{1}{N}\left\{\tfrac{1}{2}\left[[G_1(x_m,p_n)]^{\frac{M}{2}}+[G_2(x_m,p_n)]^{\frac{M}{2}}\right]\right\}^{\frac{N}{M}} \quad . \tag{7}$$

The reference ray depends on exponent M which controls the averaging of the S–wave eigenvalues of the Christoffel matrix. The reference ray is independent of exponent N. Refer to Klimeš (2006) for the calculation of the reference ray and other reference quantities.

Anisotropic–ray–theory travel times $\tau^{(1)}$ and $\tau^{(2)}$ with corresponding S–wave eigenvectors $g_i^{(1)}$ and $g_i^{(2)}$ of the Christoffel matrix are usually approximated by various perturbation expansions along the reference rays (Klimeš, 2002; 2010). The perturbation approximation of the anisotropic–ray–theory travel times depends on the reference ray and on degree N of the perturbation Hamiltonian function homogeneous with respect to the slowness vector. We choose perturbation Hamiltonian function

$$H(x_m,p_n,f_K)=\tfrac{1}{N}[G_1(x_m,p_n)]^{\frac{N}{2}}f_1+\tfrac{1}{N}[G_2(x_m,p_n)]^{\frac{N}{2}}f_2+H(x_m,p_n)(1-f_1-f_2) \tag{8}$$

linear with respect to perturbation parameters f_1 and f_2, but other authors may choose other perturbation Hamiltonian functions. Different perturbation Hamiltonian functions yield different anisotropic–ray–theory travel times $\tau^{(1)}$, $\tau^{(2)}$ and differently accurate Christoffel matrices with their eigenvectors $g_i^{(1)}$, $g_i^{(2)}$.

For the calculation of the reference ray, we usually use the reference Hamiltonian function which is the average of the homogeneous Hamiltonian functions of degree $M=-1$ with respect to the slowness vector. Note that the perturbation expansions along reference rays calculated with $M=-1$ and $M=2$ have been compared by Bulant & Klimeš (2008, tables 7, 8, 9 and 10, 11, 12). The perturbation usually yields the best results for the perturbation Hamiltonian function homogeneous of degree $N=-1$ with respect to the slowness vector.

3. Single–frequency approximation of the coupling ray theory

In the vicinity of the prevailing circular frequency ω_0, we wish to approximate propagator matrix $\mathbf{\Pi}=\mathbf{\Pi}(\omega)$ by matrix

$$\widetilde{\mathbf{\Pi}}(\omega)=\mathbf{\Pi}^{(1)}\exp(-\mathrm{i}\Delta\omega\, D)+\mathbf{\Pi}^{(2)}\exp(\mathrm{i}\Delta\omega\, D) \quad , \tag{9}$$

where

$$\Delta\omega=\omega-\omega_0 \quad , \tag{10}$$

$D=D(\omega_0)$, $\mathbf{\Pi}^{(1)}=\mathbf{\Pi}^{(1)}(\omega_0)$ and $\mathbf{\Pi}^{(2)}=\mathbf{\Pi}^{(2)}(\omega_0)$. This decomposition represents the approximation of propagator matrix $\mathbf{\Pi}=\mathbf{\Pi}(\omega)$ by two S waves with travel times $\overline{\tau}-D$ and $\overline{\tau}+D$.

We require that

$$\widetilde{\mathbf{\Pi}}(\omega_0)=\mathbf{\Pi}(\omega_0) \tag{11}$$

and

$$\frac{\partial\widetilde{\mathbf{\Pi}}}{\partial\omega}(\omega_0)=\mathbf{D}(\omega_0) \quad , \tag{12}$$

where

$$\mathbf{D}(\omega) = \frac{\partial \mathbf{\Pi}}{\partial \omega}(\omega) \quad . \tag{13}$$

Analogously to the anisotropic ray theory, we shall assume that the 2×2 matrices $\mathbf{\Pi}^{(1)}$ and $\mathbf{\Pi}^{(2)}$ are dyadic products of vectors,

$$\det\bigl(\mathbf{\Pi}^{(1)}\bigr) = 0 \quad \wedge \quad \det\bigl(\mathbf{\Pi}^{(2)}\bigr) = 0 \quad . \tag{14}$$

3.1. Determining the coefficients of single–frequency approximation (9)

We now determine coefficients D, $\mathbf{\Pi}^{(1)}$ and $\mathbf{\Pi}^{(2)}$ of the single–frequency approximation (9) of the coupling ray theory from conditions (11), (12) and (14).

We differentiate definition (9) and obtain

$$\frac{\partial \widetilde{\mathbf{\Pi}}(\omega)}{\partial \omega} = \bigl[- \mathbf{\Pi}^{(1)} \exp(-\mathrm{i}\Delta\omega\, D) + \mathbf{\Pi}^{(2)} \exp(\mathrm{i}\Delta\omega\, D)\bigr]\, \mathrm{i}\, D \quad . \tag{15}$$

Equations (11) and (12) then read

$$\mathbf{\Pi}^{(1)} + \mathbf{\Pi}^{(2)} = \mathbf{\Pi}(\omega_0) \tag{16}$$

and

$$\bigl[- \mathbf{\Pi}^{(1)} + \mathbf{\Pi}^{(2)}\bigr]\, \mathrm{i}\, D = \mathbf{D}(\omega_0) \quad . \tag{17}$$

All 2×2 matrices satisfying identities (14) satisfy relation

$$\det\bigl(\mathbf{\Pi}^{(1)} - \mathbf{\Pi}^{(2)}\bigr) = -\det\bigl(\mathbf{\Pi}^{(1)} + \mathbf{\Pi}^{(2)}\bigr) \quad . \tag{18}$$

Since matrix (16) is unimodular, we have

$$\det\bigl(\mathbf{\Pi}^{(1)} - \mathbf{\Pi}^{(2)}\bigr) = -1 \quad . \tag{19}$$

The determinants of matrices (17) then yield

$$D^2 = \det[\mathbf{D}(\omega_0)] \quad . \tag{20}$$

Without loss of generality, we may choose positive solution

$$D = \sqrt{\det[\mathbf{D}(\omega_0)]} \quad . \tag{21}$$

Equations (16) and (17) then yield

$$\mathbf{\Pi}^{(1)} = \frac{1}{2}\left[\mathbf{\Pi}(\omega_0) + \mathrm{i}\frac{\mathbf{D}(\omega_0)}{D}\right] \tag{22}$$

and

$$\mathbf{\Pi}^{(2)} = \frac{1}{2}\left[\mathbf{\Pi}(\omega_0) - \mathrm{i}\frac{\mathbf{D}(\omega_0)}{D}\right] \quad . \tag{23}$$

The single–frequency approximation (9) of the coupling ray theory is determined by coefficients (21)–(23).

3.2. Pauli matrices and assumption (14)

In this section, we propose a convenient numerical representation of matrices $\mathbf{\Pi}$, $\mathbf{D}$, $\mathbf{\Pi}^{(1)}$ or $\mathbf{\Pi}^{(2)}$. We also employ this representation in demonstrating that the 2×2 matrices (22) and (23) satisfy our assumption (14). This section may be skipped without losing the thread of the account.

The Pauli matrices are 2×2 matrices

$$\boldsymbol{\sigma}_1 = \begin{pmatrix} 0 & 1 \\ 1 & 0 \end{pmatrix} \quad , \quad \boldsymbol{\sigma}_2 = \begin{pmatrix} 0 & -\mathrm{i} \\ \mathrm{i} & 0 \end{pmatrix} \quad , \quad \boldsymbol{\sigma}_3 = \begin{pmatrix} 1 & 0 \\ 0 & -1 \end{pmatrix} \quad . \tag{24}$$

They satisfy relations

$$\boldsymbol{\sigma}_1\boldsymbol{\sigma}_2 = -\boldsymbol{\sigma}_2\boldsymbol{\sigma}_1 = \mathrm{i}\boldsymbol{\sigma}_3 \ , \quad \boldsymbol{\sigma}_2\boldsymbol{\sigma}_3 = -\boldsymbol{\sigma}_3\boldsymbol{\sigma}_2 = \mathrm{i}\boldsymbol{\sigma}_1 \ , \quad \boldsymbol{\sigma}_3\boldsymbol{\sigma}_1 = -\boldsymbol{\sigma}_1\boldsymbol{\sigma}_3 = \mathrm{i}\boldsymbol{\sigma}_2 \tag{25}$$

and

$$\boldsymbol{\sigma}_1\boldsymbol{\sigma}_1 = \boldsymbol{\sigma}_2\boldsymbol{\sigma}_2 = \boldsymbol{\sigma}_3\boldsymbol{\sigma}_3 = \mathbf{1} \quad . \tag{26}$$

The coefficient matrix of coupling equation (1) is a linear combination of matrices $\mathrm{i}\boldsymbol{\sigma}_2$ and $\mathrm{i}\boldsymbol{\sigma}_3$ with real–valued coefficients. The initial value of propagator matrix $\mathbf{\Pi}$ is $\mathbf{1}$. Because of relations (25) and (26), matrix $\mathbf{\Pi}$ can then be expressed as the linear combination

$$\mathbf{\Pi} = \Pi_0\,\mathbf{1} + \mathrm{i}\,\Pi_k\,\boldsymbol{\sigma}_k \tag{27}$$

of the Pauli matrices (24) and identity matrix $\mathbf{1}$, with real–valued coefficients Π_0 and Π_k. We insert the Pauli matrices (24) into linear combination (27) and obtain

$$\mathbf{\Pi} = \begin{pmatrix} \Pi_0 + \mathrm{i}\Pi_3 & \Pi_2 + \mathrm{i}\Pi_1 \\ -\Pi_2 + \mathrm{i}\Pi_1 & \Pi_0 - \mathrm{i}\Pi_3 \end{pmatrix} \quad . \tag{28}$$

The determinant of this matrix reads

$$\det(\mathbf{\Pi}) = \Pi_0^2 + \Pi_1^2 + \Pi_2^2 + \Pi_3^2 \quad . \tag{29}$$

Since matrix $\mathbf{\Pi}$ is unimodular, the real–valued coefficients satisfy identity

$$\Pi_0^2 + \Pi_1^2 + \Pi_2^2 + \Pi_3^2 = 1 \quad . \tag{30}$$

We now prove that our assumption (14) holds. The derivative (13) of matrix (28) reads

$$\mathbf{D} = \begin{pmatrix} D_0 + \mathrm{i}D_3 & D_2 + \mathrm{i}D_1 \\ -D_2 + \mathrm{i}D_1 & D_0 - \mathrm{i}D_3 \end{pmatrix} \quad , \tag{31}$$

where

$$D_0 = \frac{\partial \Pi_0}{\partial \omega} \quad , \qquad D_k = \frac{\partial \Pi_k}{\partial \omega} \quad . \tag{32}$$

The differentiation of identity (30) with respect to ω yields identity

$$\Pi_0 D_0 + \Pi_1 D_1 + \Pi_2 D_2 + \Pi_3 D_3 = 0 \quad . \tag{33}$$

We insert matrices (28) and (31) into expressions (22) and (23), respectively. Analogously to (29), the determinants of matrices (22) and (23) then read

$$\det\bigl(\mathbf{\Pi}^{(1,2)}\bigr) = \frac{1}{4}\left[\left(\Pi_0 \pm \mathrm{i}\frac{D_0}{D}\right)^2 + \left(\Pi_1 \pm \mathrm{i}\frac{D_1}{D}\right)^2 + \left(\Pi_2 \pm \mathrm{i}\frac{D_2}{D}\right)^2 + \left(\Pi_3 \pm \mathrm{i}\frac{D_3}{D}\right)^2\right] . \tag{34}$$

Equation (34) with identity (33) yields

$$\det\bigl(\mathbf{\Pi}^{(1,2)}\bigr) = \tfrac{1}{4}\bigl[\Pi_0^2 + \Pi_1^2 + \Pi_2^2 + \Pi_3^2 - (D_0^2 + D_1^2 + D_2^2 + D_3^2)/D^2\bigr] \quad , \tag{35}$$

which is equivalent to relation

$$\det\bigl(\mathbf{\Pi}^{(1,2)}\bigr) = \tfrac{1}{4}\bigl[\det(\mathbf{\Pi}) - \det(\mathbf{D}/D)\bigr] \quad . \tag{36}$$

Since both matrices $\mathbf{\Pi}$ and $\mathbf{D}/D$ are unimodular, we see that

$$\det\bigl(\mathbf{\Pi}^{(1,2)}\bigr) = 0 \tag{37}$$

as we have assumed.

Note that we need to calculate just one column of matrices (28) or (31). This column simultaneously determines the other column. Note also that (28) and (31) are useful numerical representations of matrices $\mathbf{\Pi}$ and $\mathbf{D}$ in terms of real–valued coefficients Π_0, Π_k and D_0, D_k.

3.3. Single–frequency approximation of the propagator matrix

If we insert matrices (22) and (23) into the approximate propagator matrix (9), we obtain relation

$$\widetilde{\mathbf{\Pi}}(\omega) = \mathbf{\Pi}(\omega_0)\cos(D\,\Delta\omega) + \frac{\mathbf{D}(\omega_0)}{D}\sin(D\,\Delta\omega) \quad . \tag{38}$$

3.4. Single–frequency approximation of the Green tensor

We now approximate propagator matrix $\Pi_{KL}(\mathbf{x}, \mathbf{x}_0, \omega)$ in the Green tensor (5) by single–frequency approximation (9). After this insertion, the coupling–ray–theory Green tensor (5) may be approximated by the superposition

$$G_{ij}(\mathbf{x}, \mathbf{x}_0, \omega) \approx G_{ij}^{(1)}(\mathbf{x}, \mathbf{x}_0, \omega) + G_{ij}^{(2)}(\mathbf{x}, \mathbf{x}_0, \omega) \tag{39}$$

of two S–wave Green tensors

$$G_{ij}^{(J)}(\mathbf{x}, \mathbf{x}_0, \omega) = A_{ij}^{(J)}(\mathbf{x}, \mathbf{x}_0, \omega_0)\exp\bigl[\mathrm{i}\omega T^{(J)}(\mathbf{x}, \mathbf{x}_0, \omega_0)\bigr] \quad , \qquad J = 1, 2 \quad . \tag{40}$$

These S waves have coupling–ray–theory travel times

$$T^{(1)}(\mathbf{x}, \mathbf{x}_0, \omega_0) = \overline{\tau}(\mathbf{x}, \mathbf{x}_0) - D(\mathbf{x}, \mathbf{x}_0, \omega_0) \tag{41}$$

and

$$T^{(2)}(\mathbf{x}, \mathbf{x}_0, \omega_0) = \overline{\tau}(\mathbf{x}, \mathbf{x}_0) + D(\mathbf{x}, \mathbf{x}_0, \omega_0) \quad . \tag{42}$$

The corresponding vectorial amplitudes are

$$A_{ij}^{(1)}(\mathbf{x}, \mathbf{x}_0, \omega^0) = A(\mathbf{x}, \mathbf{x}_0)\; g_i^{(K)}(\mathbf{x})\, g_j^{(L)}(\mathbf{x}_0)\, \Pi_{KL}^{(1)}(\mathbf{x}, \mathbf{x}_0, \omega_0)\exp[\mathrm{i}\omega_0 D(\mathbf{x}, \mathbf{x}_0, \omega_0)] \tag{43}$$

and

$$A_{ij}^{(2)}(\mathbf{x}, \mathbf{x}_0, \omega^0) = A(\mathbf{x}, \mathbf{x}_0)\; g_i^{(K)}(\mathbf{x}) g_j^{(L)}(\mathbf{x}_0)\, \Pi_{KL}^{(2)}(\mathbf{x}, \mathbf{x}_0, \omega_0)\exp[-\mathrm{i}\omega_0 D(\mathbf{x}, \mathbf{x}_0, \omega_0)] \quad . \tag{44}$$

Whereas propagator matrix $\mathbf{\Pi} = \mathbf{\Pi}(\omega)$ in the Green tensor (5) is strongly frequency dependent at high frequencies, the frequency dependence of the coupling–ray–theory travel times (41)–(42) and corresponding amplitudes (43)–(44) is likely to be moderate.

4. Numerical algorithm

We calculate propagator matrix $\mathbf{\Pi} = \mathbf{\Pi}(\omega)$ as the product of propagator matrices $\Delta\mathbf{\Pi}_k$ along short ray segments indexed $k = 1, 2, ..., K$:

$$\mathbf{\Pi} = \Delta\mathbf{\Pi}_K \, \Delta\mathbf{\Pi}_{K-1} \cdots \Delta\mathbf{\Pi}_2 \, \Delta\mathbf{\Pi}_1 \quad . \tag{45}$$

In the standard coupling ray theory, this multiplication is calculated for many frequencies. In the single–frequency approximation, the multiplication is calculated just for circular frequency $\omega = \omega_0$. The simple algorithm of multiplication (45) reads

$$\mathbf{\Pi}_0 = \mathbf{1} \quad , \tag{46}$$

$$\mathbf{\Pi}_k = \Delta\mathbf{\Pi}_k \mathbf{\Pi}_{k-1} \quad , \qquad k = 1, 2, ..., K \quad , \tag{47}$$

$$\mathbf{\Pi} = \mathbf{\Pi}_K \quad . \tag{48}$$

The individual propagator matrices are approximated by the method of mean coefficients (Červený, 2001, eq. 5.4.86; Bulant & Klimeš, 2002, eq. 17),

$$\Delta\mathbf{\Pi}_k = \mathbf{1} \cos(\alpha_k) + \mathbf{A}_k \sin(\alpha_k) \quad , \tag{49}$$

where

$$\mathbf{A}_k = \begin{pmatrix} 0 & 1 \\ -1 & 0 \end{pmatrix} \frac{\Delta\varphi_k}{\alpha_k} - \begin{pmatrix} \mathrm{i} & 0 \\ 0 & -\mathrm{i} \end{pmatrix} \frac{\Delta\varepsilon_k}{\alpha_k} \tag{50}$$

with

$$\alpha_k = \sqrt{(\Delta\varphi_k)^2 + (\Delta\varepsilon_k)^2} \quad . \tag{51}$$

Quantities $\Delta\varphi_k$ and $\Delta\varepsilon_k$ are calculated according to Bulant & Klimeš (2002, eqs. 18 and 21), but often using the second–order perturbations of travel times instead of the first–order perturbations (Klimeš & Bulant, 2006).

We obtain the algorithm of calculating the frequency derivative $\mathbf{D}$ of propagator matrix $\mathbf{\Pi}$ by differentiating algorithm (46)–(48) with respect to frequency ω:

$$\mathbf{D}_0 = \mathbf{0} \quad , \tag{52}$$

$$\mathbf{D}_k = \Delta\mathbf{\Pi}_k \mathbf{D}_{k-1} + \Delta\mathbf{D}_k \mathbf{\Pi}_{k-1} \quad , \qquad k = 1, 2, ..., K \quad , \tag{53}$$

$$\mathbf{D} = \mathbf{D}_K \quad . \tag{54}$$

The derivatives

$$\Delta\mathbf{D}_k = \frac{\partial \Delta\mathbf{\Pi}_k}{\partial\omega} \tag{55}$$

of matrices (49) read

$$\Delta\mathbf{D}_k = \left\{ \left[-\mathbf{1} \sin(\alpha_k) + \mathbf{A}_k \cos(\alpha_k) - \mathbf{A}_k \frac{\sin(\alpha_k)}{\alpha_k} \right] \frac{\Delta\varepsilon_k}{\alpha_k} - \begin{pmatrix} \mathrm{i} & 0 \\ 0 & -\mathrm{i} \end{pmatrix} \frac{\sin(\alpha_k)}{\alpha_k} \right\} \frac{\Delta\varepsilon_k}{\omega} \ . \tag{56}$$

5. Numerical examples

The single–frequency approximation of the coupling ray theory has been coded as a new option of program `green.for` of package CRT (Bucha & Bulant, 2012). Program `green.for` now allows synthetic seismograms of coupled S–waves in weakly anisotropic velocity models to be calculated using either the standard frequency–domain coupling ray theory or its single–frequency approximation. In this paper, the single–frequency approximation of the coupling ray theory is numerically tested in eight weakly anisotropic velocity models. These anisotropic velocity models with related input data can be found in package DATA (Bucha & Bulant, 2012).

5.1. Numerical methods which are compared

In the presented numerical examples, we follow the work of Pšenčík, Farra & Tessmer (2011; 2012), who compared the synthetic seismograms calculated by their approximation of the coupling ray theory with the synthetic seismograms generated by the Fourier pseudospectral method. Bulant et al. (2011) then numerically compared three different approximations of the coupling ray theory with the Fourier pseudospectral method.

In this paper, we compare the synthetic seismograms calculated by three numerical methods: (a) the proposed *single–frequency approximation* of the coupling ray theory; (b) the *standard coupling ray theory* calculated for all frequencies according to the algorithm of Bulant & Klimeš (2002); (c) the *Fourier pseudospectral method* which is considered here as a nearly exact reference. Refer to Pšenčík, Farra & Tessmer (2011; 2012) for the description of the Fourier pseudospectral method used here.

Both the coupling ray theory and its single–frequency approximation are calculated along anisotropic common reference rays (Klimeš, 2006). For the calculation of the reference rays, we use reference Hamiltonian function (7) which is the average of the homogeneous Hamiltonian functions of degree $M = -1$ with respect to the slowness vector. For perturbations, we use perturbation Hamiltonian function (8) which is homogeneous of degree $N = -1$ with respect to the slowness vector. We approximate the anisotropic–ray–theory travel times $\tau^{(1)}$ and $\tau^{(2)}$ in the coupling equation by the second–order perturbation expansion according to Klimeš & Bulant (2006). We approximate eigenvectors $g_i^{(1)}$ and $g_i^{(2)}$ of the Christoffel matrix by the unperturbed reference eigenvectors calculated using the Christoffel matrix with the unperturbed reference slowness vector, although we know that we should calculate them better using the Christoffel matrix with the first–order perturbation expansion of the slowness vector.

5.2. Anisotropic velocity models

We consider eight weakly anisotropic velocity models referred to as QIH, QI, QI2, QI4, SC1_I, SC1_II, KISS and ORT. All these velocity models are laterally homogeneous. The density is constant. The elastic moduli are linear functions of depth.

A vertically heterogeneous 1–D anisotropic velocity model QI was provided by Pšenčík & Dellinger (2001, model WA rotated by 45°), who performed the coupling–ray–theory calculations using the programs of package ANRAY (Pšenčík, 1998) and compared the results with the reflectivity method. The same velocity model has been used by Bulant & Klimeš (2002) and Klimeš & Bulant (2004) to demonstrate the coupling ray theory and its quasi–isotropic approximations. For comparison with the isotropic–ray–theory and anisotropic–ray–theory seismograms in velocity model QI and for a more

detailed discussion and description of this velocity model refer to Pšenčík & Dellinger (2001). Velocity model QI is transversely isotropic in a vertical plane which forms a 45° angle with the source–receiver vertical plane.

Velocity models QIH, QI2 and QI4 are derived from velocity model QI and mutually differ by their degrees of anisotropy. The differences of the elastic moduli in velocity models QIH, QI, QI2 and QI4 from the elastic moduli in the reference isotropic velocity model are determined by ratio $0.5 : 1 : 2 : 4$. For the elastic moduli in velocity models QI, QI2 and QI4 refer to Bulant & Klimeš (2008).

For the description of velocity models SC1_I, SC1_II, KISS and ORT and for the comparison with the anisotropic–ray–theory seismograms in these velocity models refer to Pšenčík, Farra & Tessmer (2011; 2012).

At the depth of 0 km, velocity model SC1_I is transversely isotropic and its axis of symmetry is horizontal. At this depth, the slowness surface contains an intersection singularity, whereas velocity models QIH, QI, QI2 and QI4 display no intersection singularity. At the depth of 1.5 km, velocity model SC1_I is very close to isotropic, but is slightly cubic and its symmetry axes coincide with the coordinate axes. This means that, at depths between 0 km and 1.5 km, velocity model SC1_I is very close to transversely isotropic, but is slightly tetragonal. Whereas the transversely isotropic medium contains the intersection singularity through which the rays pass without rotation of the eigenvectors of the Christoffel matrix, in the slightly tetragonal medium, the S–wave slowness surface is split at this unstable singularity (Crampin, 1981) and the S–wave polarizations rapidly rotate by 90° there. This split intersection singularity then acts as an interface and approximately converts the S–wave polarizations from S1 to S2, and vice versa.

Velocity model SC1_II is analogous to SC1_I, but the axis of symmetry of its transversely isotropic component is tilted. The symmetry axes of its weak cubic component coincide with the coordinate axes. Velocity model SC1_II does not display the split intersection singularity in the source–receiver plane. The deviation of the rays from the source–receiver plane is much greater in velocity model SC1_II than in velocity model SC1_I (Pšenčík, Farra & Tessmer, 2011; 2012).

Velocity model KISS represents velocity model QI described above, rotated by $-44°$ in order to position the axis of symmetry, corresponding to the kiss S–wave singularity, just 1° from the source–receiver plane.

In the weakly orthorhombic velocity model ORT, the slowness surface contains four conical singularities. The rays leading from the source to the middle part of the receiver profile pass close to one of these singularities. This conical singularity then acts as an interface and approximately converts the S–wave polarizations from S1 to S2, and vice versa.

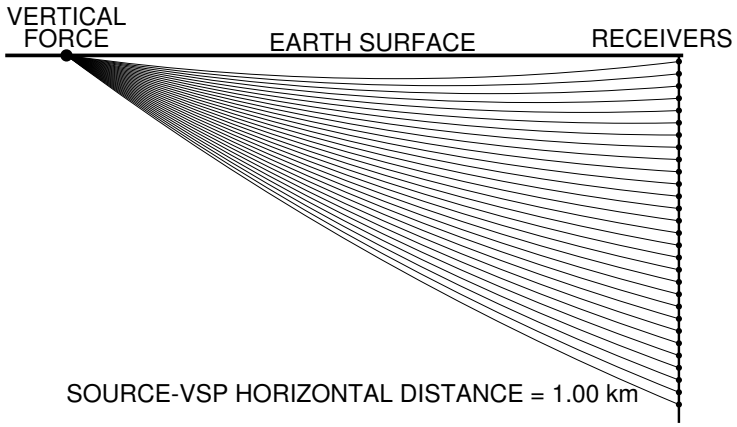

Figure 1: The source–receiver configuration for the calculation of synthetic seismograms, with a sketch of the reference rays. The source is located at the Earth's surface, the receivers are placed in the vertical well. The numbers and depths of the receivers differ for the individual velocity models and are presented in the figures with seismograms.

5.3. Measurement configuration

The synthetic seismograms generated by a vertical force are calculated at the receivers located in a vertical well at a distance of 1 km from the source. The source–receiver configuration in velocity models QIH, QI, QI2, QI4 and KISS is displayed in Figure 1. The source–receiver configuration in velocity models SC1_I, SC1_II and ORT is similar except for different receiver positions in the vertical well.

The source time function is the Gabor signal $\cos(2\pi ft)\exp[-(2\pi ft/4)^2]$ with reference frequency $f = 50$ Hz, bandpass filtered by a cosine filter specified by frequencies 0 Hz, 5 Hz, 60 Hz and 100 Hz. The numbers and depths of the receivers differ for the individual velocity models and are displayed in the plots of seismograms. The receivers record the following 3 components of displacement: vertical component (positive downwards), transverse component (perpendicular to the source–receiver plane), and radial component (along the line connecting the source and the top of the well, positive away from the source). The recording system is right–handed. For the single–frequency approximation of the coupling ray theory, we naturally use prevailing frequency $f_0 = 50$ Hz.

5.4. Comparison of synthetic seismograms

The synthetic seismograms in velocity models QIH, QI, QI2, QI4, SC1_I, SC1_II, KISS and ORT are displayed in Figures 2–9. In each figure, the synthetic seismograms calculated by the standard coupling ray theory and by the Fourier pseudospectral method are displayed in different colours. In each velocity model, the amplitude scaling is equal for all components and all receivers.

Note that the second (transverse) component would vanish in the isotropic–ray–theory seismograms in all these velocity models. This second component would also be quite different in the anisotropic–ray–theory seismograms in velocity models QIH (Červený, Klimeš & Pšenčík, 2007, fig. 19), QI (Pšenčík & Dellinger, 2001, fig. 8), SC1_I, SC1_II, KISS and ORT (Pšenčík, Farra & Tessmer, 2011, figs. 10, 13, 16, 19).

In all eight velocity models, the additional inaccuracy introduced by the single–frequency approximation is generally smaller than the inaccuracy of the standard frequency–domain coupling ray theory. The synthetic seismograms calculated by the single–frequency approximation of the coupling ray theory are plotted in red, and

are often obscured by the standard–coupling–ray–theory seismograms plotted in green (in black in Figure 2). The additional inaccuracy introduced by the single–frequency approximation is most pronounced in velocity model QI2 (Figure 4) and is mostly invisible or even completely invisible in the other 7 velocity models.

In velocity model QIH (Figure 2), we have the results of the standard coupling ray theory and of its single–frequency approximation only. We can observe very good agreement between the single–frequency approximation seismograms and the standard–coupling–ray–theory seismograms. The dependence between the strength of the anisotropy and the differences of both the coupling–ray–theory seismograms from the Fourier pseudospectral seismograms can be observed in Figures 3–5. From this dependence, we may estimate that the accuracy of both the coupling–ray–theory seismograms in velocity model QIH is very good.

In velocity model QI (Figure 3) whose anisotropy is twice stronger than in model QIH, we can again observe an overall good fit between the single–frequency approximation seismograms and the standard–coupling–ray–theory seismograms. Both these coupling–ray–theory seismograms differ from the Fourier pseudospectral seismograms only negligibly.

In velocity model QI2 (Figure 4) whose anisotropy is twice stronger than in model QI, we can observe slight differences between the single–frequency approximation seismograms and the standard–coupling–ray–theory seismograms in the second (transverse) component. This component also displays the development of S–wave splitting. We may thus conclude that the coupling of the two S waves plays an important role in this velocity model and is also related to the slight inaccuracy of the single–frequency approximation. However, the additional inaccuracy introduced by the single–frequency approximation is smaller than the inaccuracy of the standard coupling ray theory. Note that the differences of both the coupling–ray–theory seismograms from the Fourier pseudospectral seismograms increase with increasing anisotropy, see Figures 3–5.

In velocity model QI4 (Figure 5) whose anisotropy is 4 times stronger than in model QI, we can see that both the single–frequency approximation and the standard coupling ray theory perform equally well, even though the velocity model is considerably anisotropic, and the separation of the two S waves is about 0.06 s which corresponds approximately to three S–wave periods.

The slowness surface in velocity model SC1_I contains the split intersection singularity. In Figure 6, the single–frequency approximation seismograms are mostly obscured by the standard coupling ray theory seismograms. Both the coupling–ray–theory seismograms are close to the Fourier pseudospectral seismograms despite the existence of the above–mentioned intersection singularity in this velocity model.

The slowness surface in velocity model SC1_II contains the split intersection singularity analogous to velocity model SC1_I, but with a tilted axis of symmetry. The tilted split intersection singularity does not intersect the source–receiver plane. The deviation of the rays from the source–receiver plane is much greater in velocity model SC1_II than in velocity model SC1_I (Pšenčík, Farra & Tessmer, 2011; 2012). The reference eigenvectors of the Christoffel matrix thus probably cannot approximate the eigenvectors of the two S waves correctly, see the discussion in Pšenčík, Farra & Tessmer (2011; 2012). The effects of the above phenomenon can be observed in the seismograms at the shallow receivers in Figure 7. The single–frequency approximation is nearly identical to the standard coupling ray theory even in this situation.

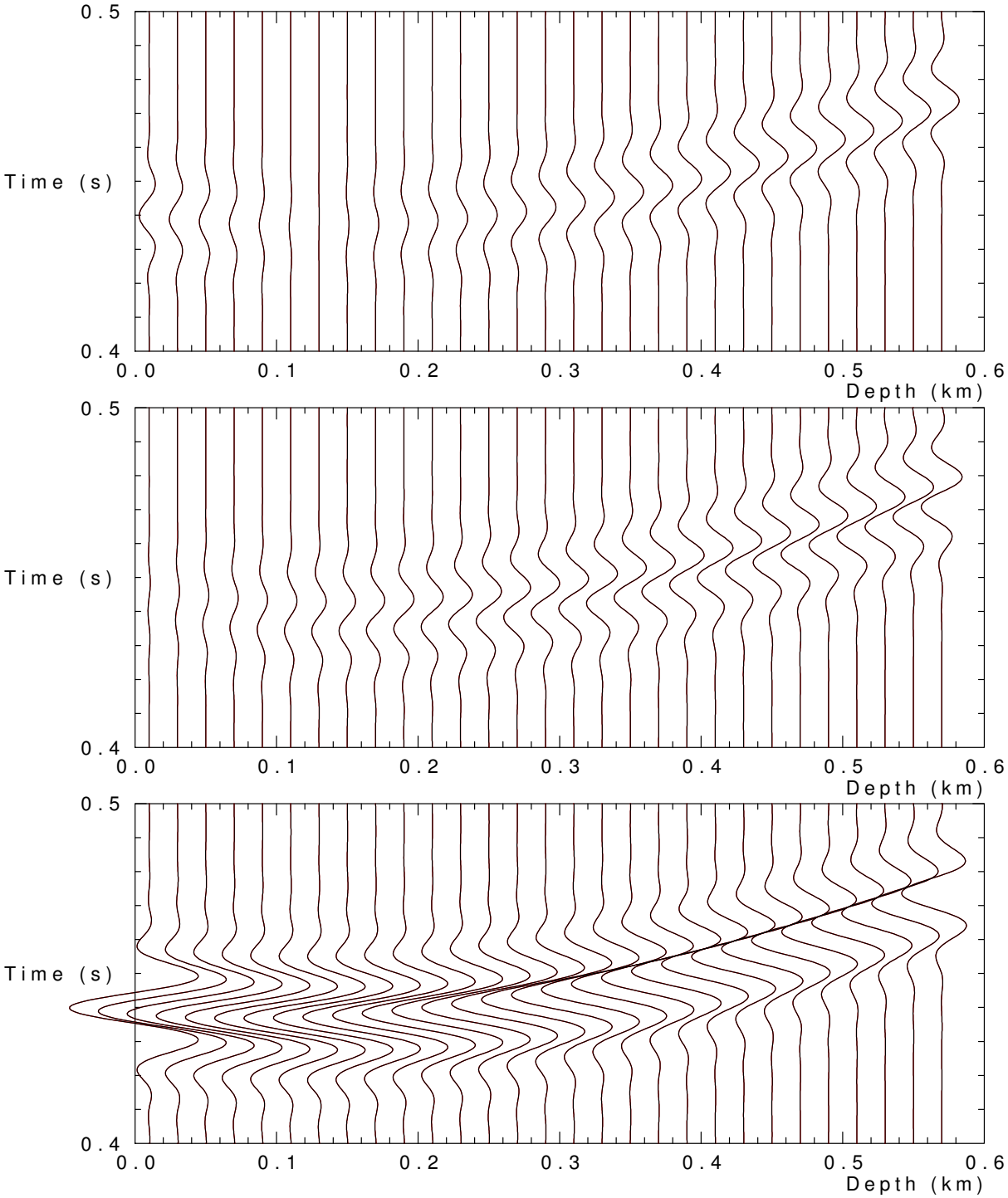

Figure 2: Radial, transverse and vertical component of the seismograms calculated in velocity model QIH. All seismograms are scaled equally. In this velocity model, we have got the results of the standard coupling ray theory and of its single–frequency approximation only. The seismograms calculated by the single–frequency approximation are plotted in **red**, and they are overlaid by the seismograms calculated by the standard–coupling–ray–theory seismograms plotted in **black**. The seismograms are in good agreement; the single–frequency approximation seismograms are obscured by the standard–coupling–ray–theory seismograms.

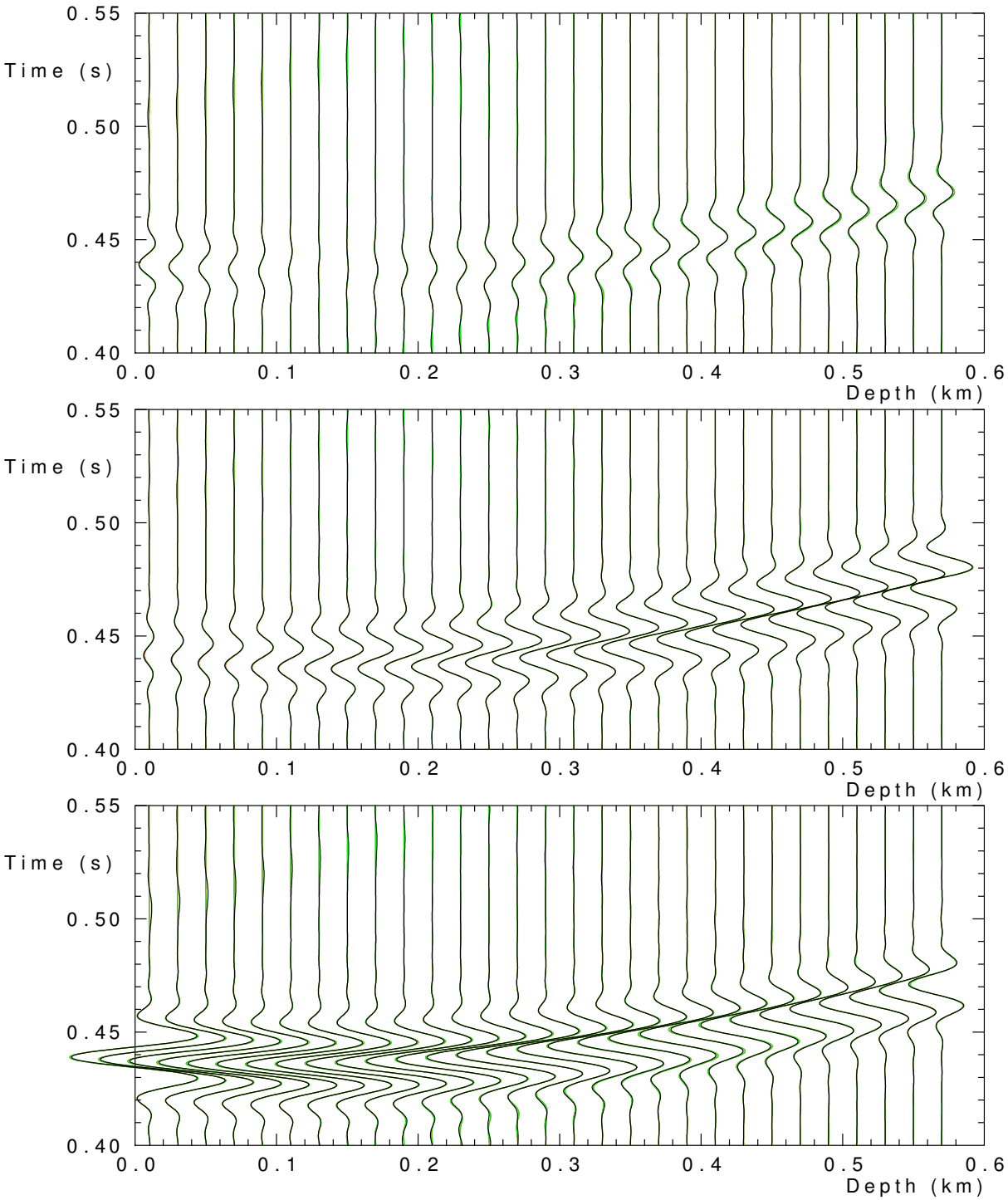

Figure 3: Radial, transverse and vertical component of the seismograms calculated in velocity model QI. The results of the single–frequency approximation are plotted in **red**, the standard–coupling–ray–theory–seismograms are then plotted in **green**, and they are overlaid by the seismograms calculated by the Fourier pseudospectral method plotted in **black**. All seismograms are in good agreement, with the single–frequency approximation seismograms obscured by the standard–coupling–ray–theory–seismograms. The wave arriving at the shallowest receivers about time 0.53 s is an artifact of the Fourier pseudospectral method.

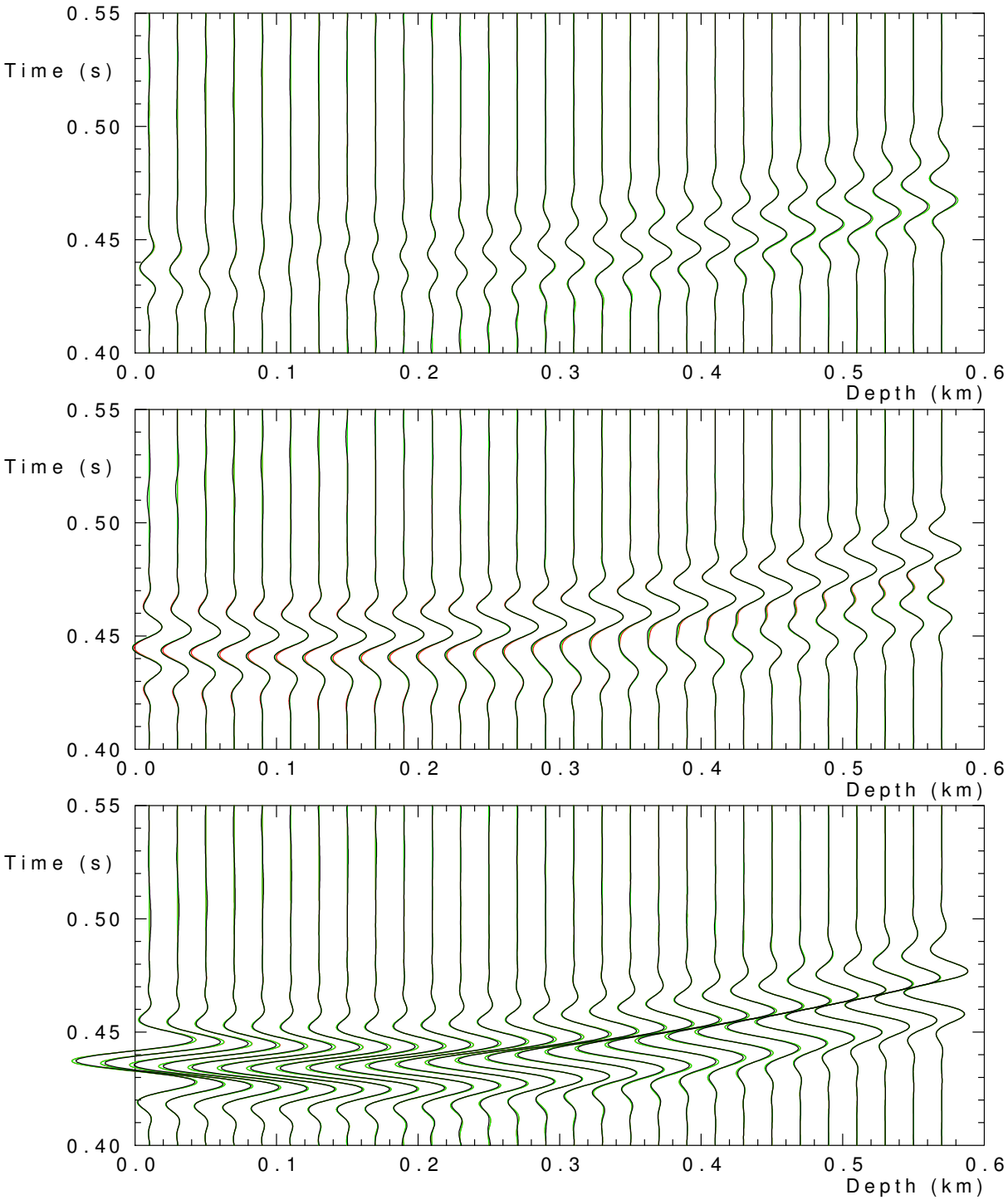

Figure 4: Radial, transverse and vertical component of the seismograms calculated in velocity model QI2. The seismograms are plotted in order **red** (single–frequency approximation), **green** (standard coupling ray theory) and **black** (Fourier pseudospectral method). All seismograms are in overall good agreement. Slight differences between the single–frequency approximation seismograms and the standard–coupling–ray–theory seismograms appear in the second (transverse) component. The second component also displays the development of S–wave splitting. We may thus conclude that the frequency–dependent coupling of the two S waves plays an important role in this velocity model and is also related to the slight inaccuracy of the single–frequency approximation.

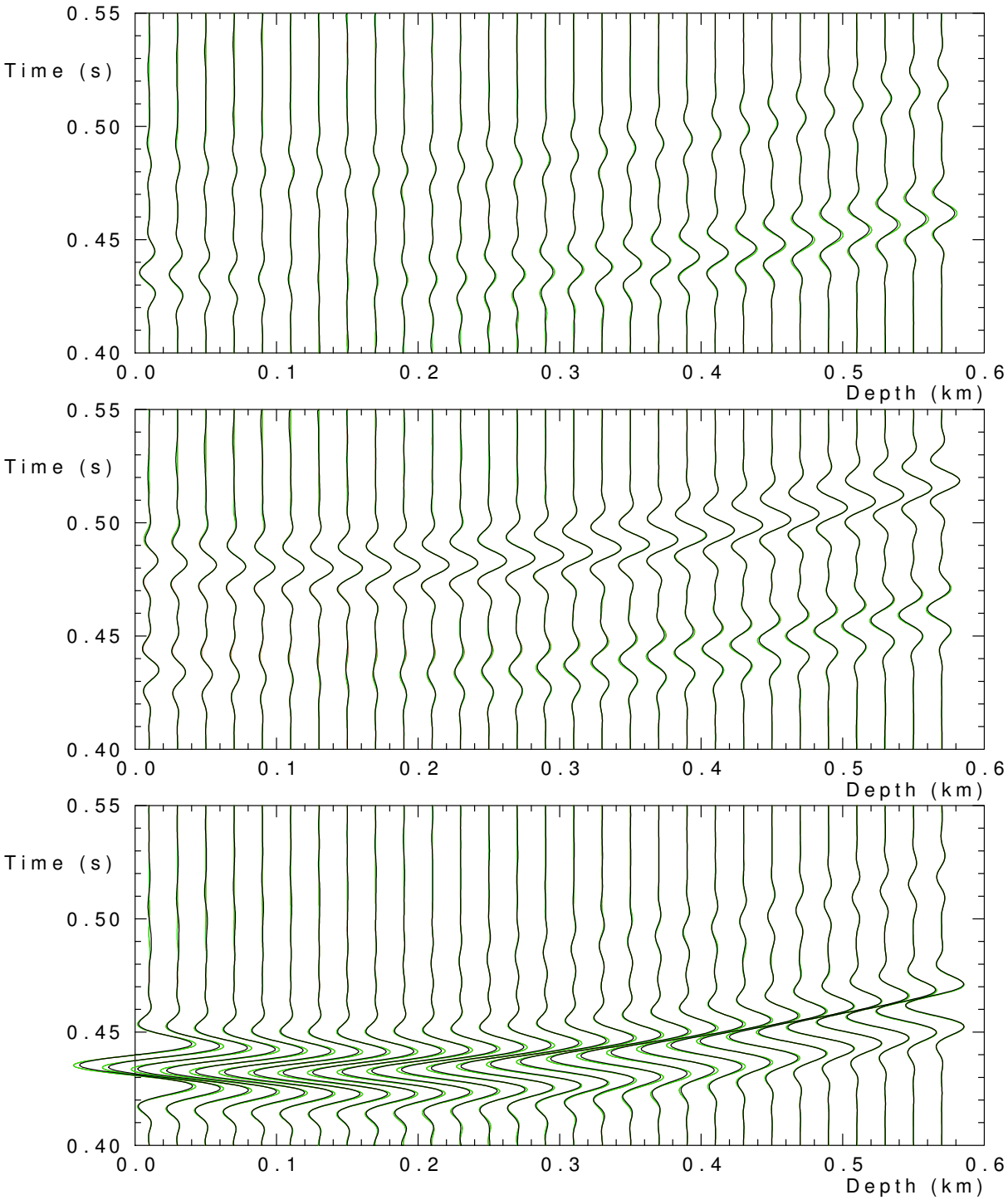

Figure 5: Radial, transverse and vertical component of the seismograms calculated in velocity model QI4. The seismograms are plotted in order **red** (single–frequency approximation), **green** (standard coupling ray theory) and **black** (Fourier pseudospectral method). The velocity model is considerably anisotropic and the two S waves are fully separated. The coupling effects are thus less pronounced, and the single–frequency approximation seismograms are in good agreement with the standard–coupling–ray–theory seismograms. The differences between both the coupling–ray–theory seismograms and the Fourier pseudospectral method are slightly higher than in the previous velocity models.

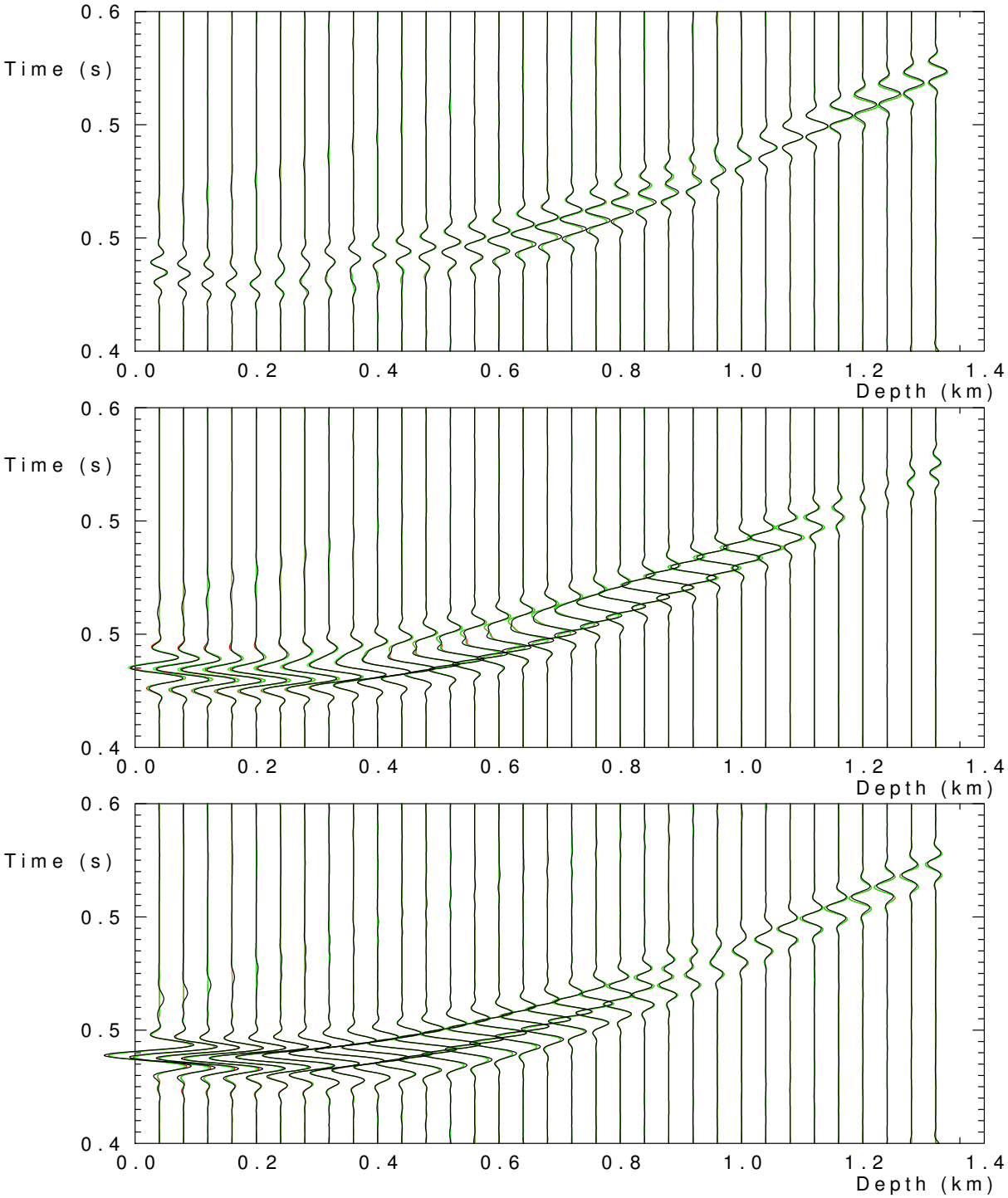

Figure 6: Radial, transverse and vertical component of the seismograms calculated in velocity model SC1_I. The seismograms are plotted in order **red** (single–frequency approximation), **green** (standard coupling ray theory) and **black** (Fourier pseudospectral method). The single–frequency approximation seismograms are mostly obscured by the standard–coupling–ray–theory seismograms. Both the coupling–ray–theory seismograms are close to the Fourier pseudospectral seismograms.

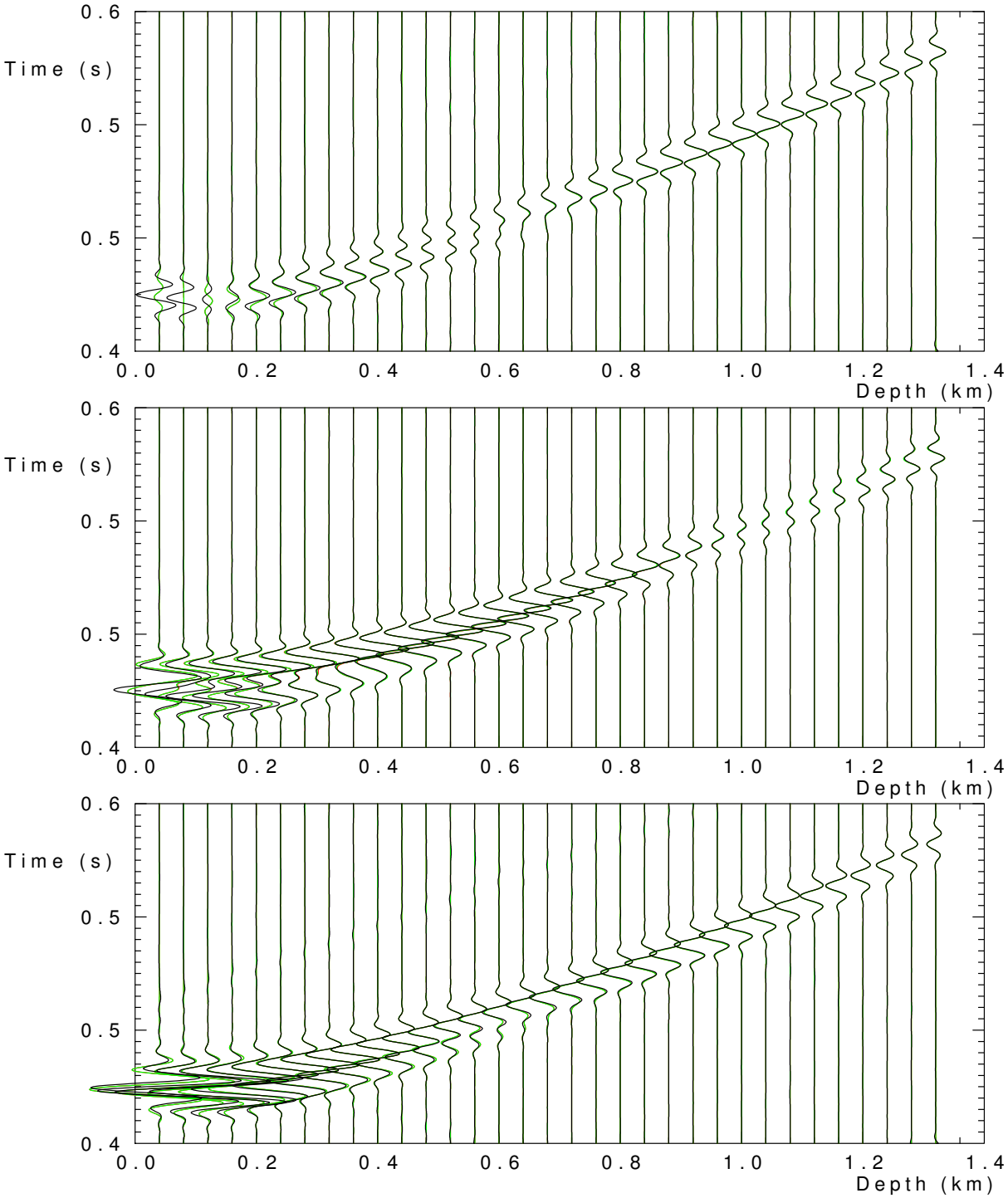

Figure 7: Radial, transverse and vertical component of the seismograms calculated in velocity model SC1_II. The seismograms are plotted in order **red** (single–frequency approximation), **green** (standard coupling ray theory) and **black** (Fourier pseudospectral method). The seismograms from the shallow receivers indicate problems with the approximation of the S–wave eigenvectors of the Christoffel matrices by the reference eigenvectors. On the other hand, the single–frequency approximation represents a very good approximation to the standard coupling ray theory even in this situation.

The slowness surface in velocity model KISS contains a kiss singularity analogous to velocity model QI, but deviated by only 1° from the source–receiver plane, instead of 45° in velocity model QI. As a consequence, the vertical force generates almost no energy in the second (transverse) component. Figure 8 shows that the differences of both the coupling–ray–theory methods from the Fourier pseudospectral method are negligible, and that the differences of the single–frequency approximation from the standard coupling ray theory are invisible.

The slowness surface in velocity model ORT contains four conical singularities. The rays leading from the source to the receivers at depths from 0.72 km to 0.92 km pass close to one of these singularities. This conical singularity then acts as an interface and approximately converts the S–wave polarizations from S1 to S2, and vice versa. In Figure 9, we can see a very good overall fit of both the single–frequency approximation seismograms and the standard–coupling–ray–theory seismograms with the Fourier pseudospectral seismograms, except for the slight differences in the singular region around the depth of 0.8 km. The differences of the single–frequency approximation from the standard coupling ray theory are invisible.

5.5. Coupling–ray–theory travel times

The coupling–ray–theory travel times (41) and (42) are often close to the anisotropic–ray–theory travel times $\tau^{(1)}$ and $\tau^{(2)}$. The most important exception is observed in velocity model ORT, at the receivers at depths from 0.72 km to 0.92 km. The rays leading from the source to these receivers pass close to the conical singularity at the slowness surface. This conical singularity then acts as an interface and approximately converts the S–wave polarizations from S1 to S2, and vice versa. The coupling–ray–theory travel times then correspond to the S1S2 and S2S1 anisotropic–ray–theory travel times of the converted waves, rather than to the S1 and S2 anisotropic–ray–theory travel times. This behaviour of the coupling–ray–theory travel times is evident in Table 1, where the differences of the coupling–ray–theory travel times (41) and (42) from the mean travel time (6) at the frequency of 50 Hz are compared with the differences of the anisotropic–ray–theory travel times $\tau^{(1)}$ and $\tau^{(2)}$ from the mean travel time (6). The coupling–ray–theory travel times at these receivers are practically frequency independent between 10 Hz and 100 Hz.

Depth	D	$\frac{1}{2}\lvert\tau^{(2)}-\tau^{(1)}\rvert$
0.72	0.003616	0.003638
0.76	0.002210	0.002536
0.80	0.000883	0.001915
0.84	0.000362	0.001748
0.88	0.001515	0.002000
0.92	0.002581	0.002634

Table 1. Receivers in velocity model ORT influenced by the conical singularity at the slowness surface. Differences D of the coupling–ray–theory travel times from the mean travel time in seconds at the frequency of 50 Hz are compared with the differences $\frac{1}{2}\lvert\tau^{(2)}-\tau^{(1)}\rvert$ of the anisotropic–ray–theory travel times from the mean travel time in seconds. The anisotropic–ray–theory travel times are calculated by the second–order perturbation expansion along the reference rays traced in steps of 0.01 s.

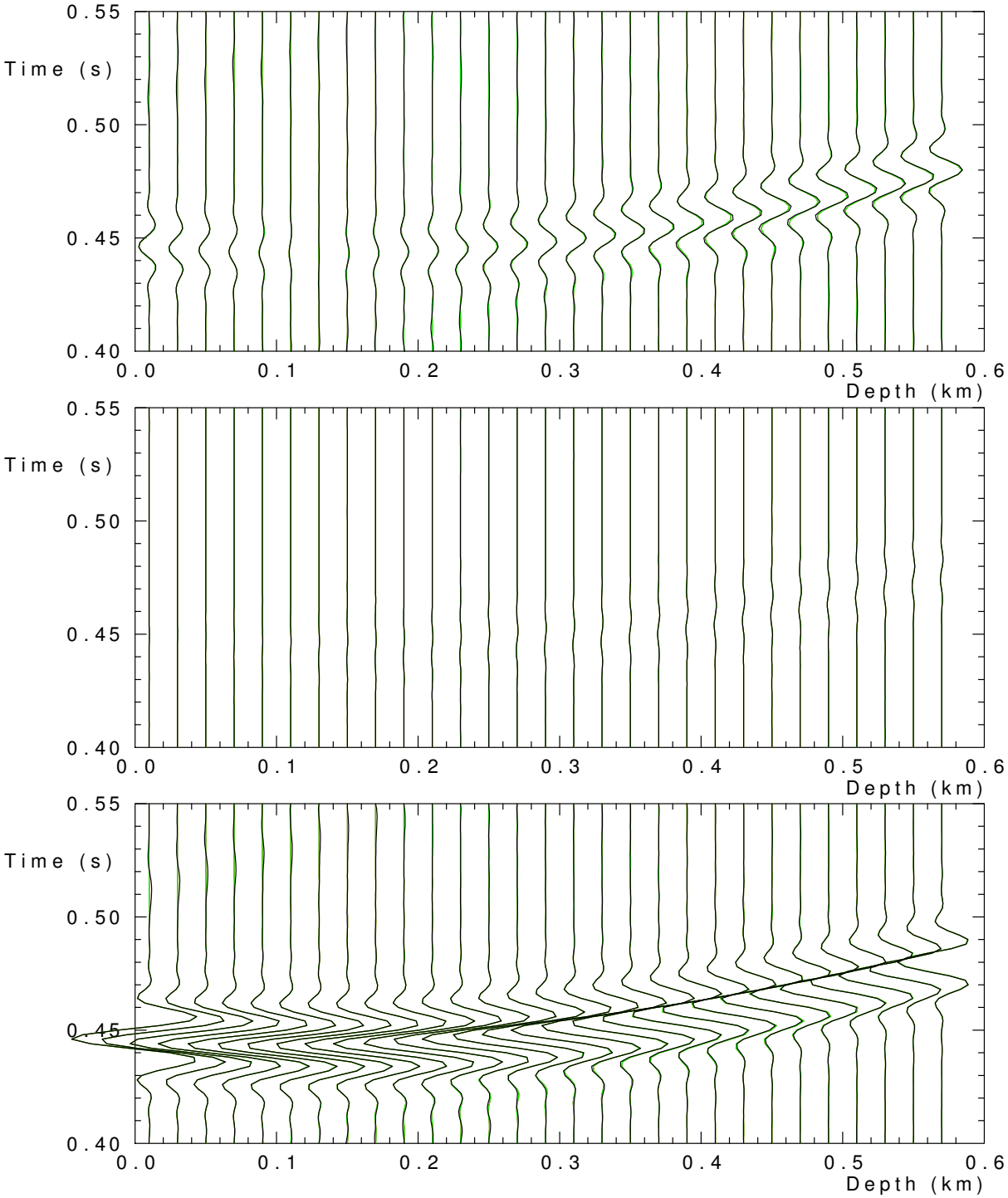

Figure 8: Radial, transverse and vertical component of the seismograms calculated in velocity model KISS. The seismograms are plotted in order **red** (single–frequency approximation), **green** (standard coupling ray theory) and **black** (Fourier pseudospectral method). All seismograms are in good agreement, similarly as in Figure 3.

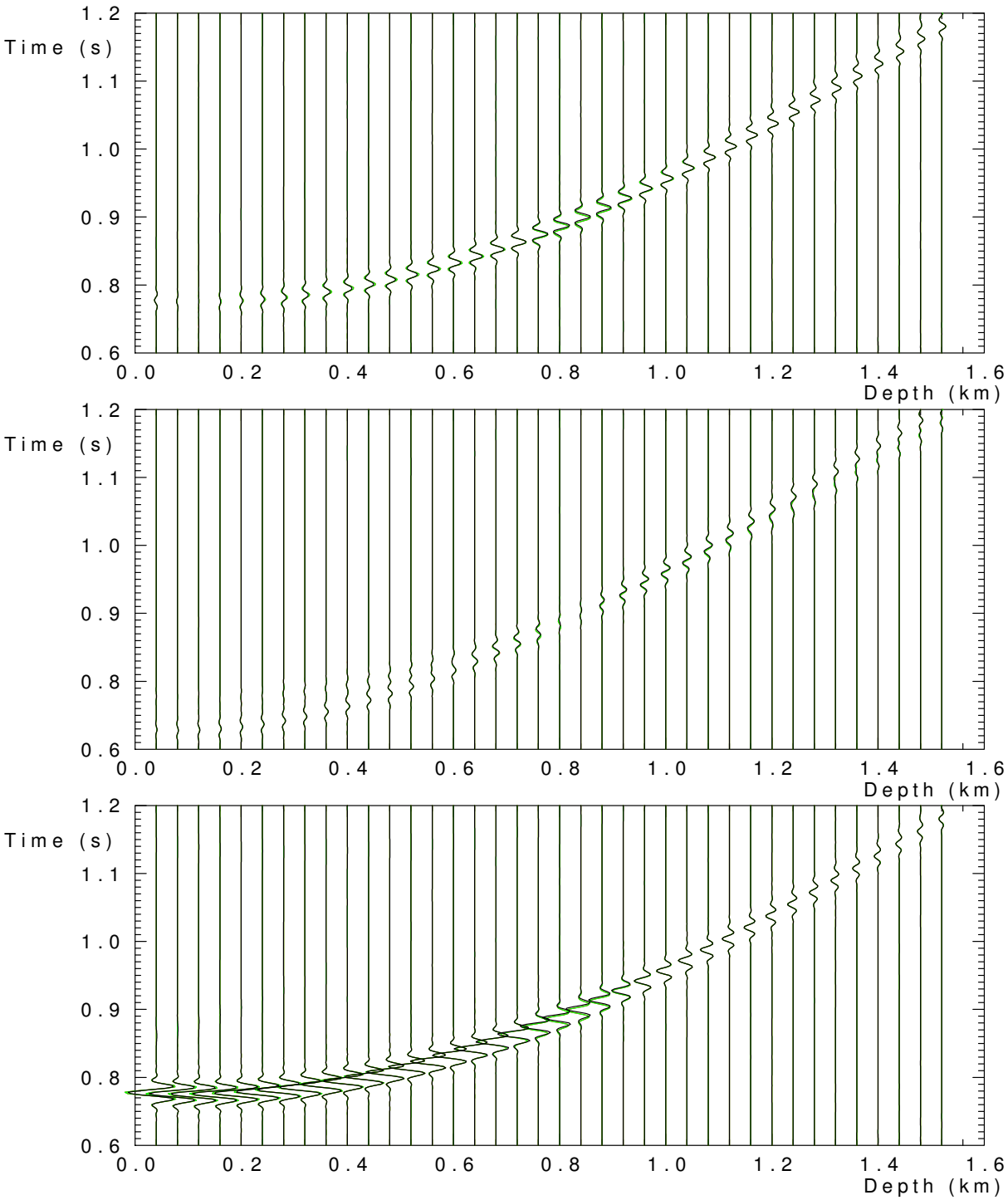

Figure 9: Radial, transverse and vertical component of the seismograms calculated in velocity model ORT. The seismograms are plotted in order **red** (single–frequency approximation), **green** (standard coupling ray theory) and **black** (Fourier pseudospectral method). The single–frequency approximation seismograms are obscured by the standard–coupling–ray–theory seismograms. Both the coupling–ray–theory seismograms are close to the Fourier pseudospectral seismograms despite the existence of conical singularities in this velocity model.

An analogous behaviour of the coupling–ray–theory travel times is also observed in velocity model SC1_I, at the deepest receivers at depths from 1.12 km to 1.32 km. The rays leading from the source to these receivers pass through the split intersection singularity at the slowness surface. This split intersection singularity then acts as an interface and approximately converts the S–wave polarizations from S1 to S2, and vice versa. The coupling–ray–theory travel times then correspond to the S1S2 and S2S1 anisotropic–ray–theory travel times of the converted waves, rather than to the S1 and S2 anisotropic–ray–theory travel times. This behaviour of the coupling–ray–theory travel times is evident in Table 2, where the differences of the coupling–ray–theory travel times (41) and (42) from the mean travel time (6) at the frequency of 50 Hz are compared with the differences of the anisotropic–ray–theory travel times $\tau^{(1)}$ and $\tau^{(2)}$ from the mean travel time (6). The coupling–ray–theory travel times at these receivers are again practically frequency independent between 10 Hz and 100 Hz.

Depth	D	$\frac{1}{2}\lvert\tau^{(2)}-\tau^{(1)}\rvert$
1.12	0.001754	0.001786
1.16	0.001104	0.001388
1.20	0.000475	0.001220
1.24	0.000130	0.001235
1.28	0.000709	0.001392
1.32	0.001262	0.001657

Table 2. Receivers in velocity model SC1_I influenced by the split intersection singularity at the slowness surface. Differences D of the coupling–ray–theory travel times from the mean travel time in seconds at the frequency of 50 Hz are compared with the differences $\frac{1}{2}|\tau^{(2)}-\tau^{(1)}|$ of the anisotropic–ray–theory travel times from the mean travel time in seconds. The anisotropic–ray–theory travel times are calculated by the second–order perturbation expansion along the reference rays traced in steps of 0.001 s.

Apart from the above mentioned singularities at the slowness surface, there are also less pronounced differences between the coupling–ray–theory travel times and the anisotropic–ray–theory travel times. As a rule, these "soft" differences approach zero with increasing frequency ω. The importance of these soft differences can be evaluated in terms of expression

$$\omega\big(\tfrac{1}{2}\big|\tau^{(2)}-\tau^{(1)}\big|-D\big) \quad . \tag{57}$$

The most important soft differences between the coupling–ray–theory travel times and the anisotropic–ray–theory travel times are observed in velocity model SC1_II, around the receiver at the depth of 0.96 km and around the frequency of 80 Hz, where the difference of the coupling–ray–theory travel time from the mean travel time is

$$D = 0.003572\,\mathrm{s} \quad , \tag{58}$$

whereas the difference of the anisotropic–ray–theory travel time from the mean travel time is

$$\tfrac{1}{2}\big|\tau^{(2)}-\tau^{(1)}\big| = 0.003767\,\mathrm{s} \quad . \tag{59}$$

The coupling–ray–theory travel times in velocity model SC1_II approach the anisotropic–ray–theory travel times with increasing frequency.

The next most important soft differences between the coupling–ray–theory travel times and the anisotropic–ray–theory travel times are observed in velocity model SC1_I,

around the receiver at the depth of 0.04 km and around the frequency of 40 Hz, where the difference of the coupling–ray–theory travel time from the mean travel time is

$$D = 0.007136\,\mathrm{s} \quad , \tag{60}$$

whereas the difference of the anisotropic–ray–theory travel time from the mean travel time is

$$\tfrac{1}{2}\left|\tau^{(2)} - \tau^{(1)}\right| = 0.007488\,\mathrm{s} \quad . \tag{61}$$

The coupling–ray–theory travel times at the shallow receivers in velocity model SC1_I approach the anisotropic–ray–theory travel times with increasing frequency.

Within frequency band 10 Hz to 100 Hz, the differences between the coupling–ray–theory travel times and the anisotropic–ray–theory travel times in velocity models QIH, QI, QI2 and QI4 are an order of magnitude less important than those in velocity model SC1_II, or at the shallow receivers in velocity model SC1_I. The coupling–ray–theory travel times approach the anisotropic–ray–theory travel times with increasing frequency.

The differences between the coupling–ray–theory travel times and the anisotropic–ray–theory travel times in velocity model ORT at the receivers outside the singular region, which extends from the depth of 0.72 km to 0.92 km, are even much smaller within the 10 Hz to 100 Hz frequency band. These coupling–ray–theory travel times approach the anisotropic–ray–theory travel times with increasing frequency.

The coupling–ray–theory travel times in velocity model KISS are equal to the anisotropic–ray–theory travel times up to rounding errors, independently of frequency within the 10 Hz to 100 Hz band.

6. Conclusions

Within a limited frequency band, we may efficiently approximate the frequency–domain coupling–ray–theory Green tensor by two Green tensors corresponding to two S waves, described by their coupling–ray–theory travel times and the corresponding vectorial amplitudes calculated for the prevailing frequency. The additional inaccuracy introduced by this single–frequency approximation is smaller than the inaccuracy of the standard frequency–domain coupling ray theory, and smaller than the additional inaccuracy introduced by many other approximations of the coupling ray theory.

The single–frequency approximation of the coupling ray theory allows us to process the coupling–ray–theory wavefield in the same way as the anisotropic–ray–theory wavefield. This simplification may be decisive when storing the Green tensor at the nodes of dense grids, which is typical for applications such as seismic migrations. The single–frequency approximation with its coupling–ray–theory travel times also offers a new way of understanding the results of the coupling ray theory.

Acknowledgements

We are indebted to Einar Iversen who always encouraged us to study this problem. Ekkehart Tessmer kindly applied his Fourier pseudospectral method to calculating the seismograms which we used here as nearly exact reference seismograms. We also thank Ivan Pšenčík for his assistance with the description of the numerical examples.

The research has been supported by the Grant Agency of the Czech Republic under contract P210/10/0736, by the Ministry of Education of the Czech Republic within research project MSM0021620860, by the European Commission under contract FP7-PEOPLE-IAPP-2009-230669 (project AIM), and by the members of the consortium "Seismic Waves in Complex 3–D Structures" (see "http://sw3d.cz").

References

Bucha, V. & Bulant, P. (eds.) (2012): SW3D–CD–16 (DVD–ROM). In: *Seismic Waves in Complex 3–D Structures, Report 22*, pp. 183–184, Dep. Geophys., Charles Univ., Prague.

Bulant, P. & Klimeš, L. (2002): Numerical algorithm of the coupling ray theory in weakly anisotropic media. *Pure appl. Geophys.*, **159**, 1419–1435.

Bulant, P. & Klimeš, L. (2008): Numerical comparison of the isotropic–common–ray and anisotropic–common–ray approximations of the coupling ray theory. *Geophys. J. int.*, **175**, 357–374.

Bulant, P., Pšenčík, I., Farra, V. & Tessmer, E. (2011): Comparison of the anisotropic–common–ray approximation of the coupling ray theory for S waves with the Fourier pseudo–spectral method in weakly anisotropic models. In: *Seismic Waves in Complex 3–D Structures, Report 21*, pp. 167–183, Dep. Geophys., Charles Univ., Prague, online at "http://sw3d.cz".

Červený, V. (2001): *Seismic Ray Theory.* Cambridge Univ. Press, Cambridge.

Červený, V., Klimeš, L. & Pšenčík, I. (2007): Seismic ray method: Recent developments. *Advances in Geophysics*, **48**, 1–126, online at "http://sw3d.cz".

Coates, R.T. & Chapman, C.H. (1990): Quasi–shear wave coupling in weakly anisotropic 3–D media. *Geophys. J. int.*, **103**, 301–320.

Crampin, S. (1981): A review of wave motion in anisotropic and cracked elastic–media. *Wave Motion*, **3**, 343–391.

Farra, V. & Pšenčík, I. (2008): First–order ray computations of coupled S waves in inhomogeneous weakly anisotropic media. *Geophys. J. int.*, **173**, 979–989.

Farra, V. & Pšenčík, I. (2010): Coupled S waves in inhomogeneous weakly anisotropic media using first–order ray tracing. *Geophys. J. int.*, **180**, 405–417.

Klimeš, L. (2002): Second–order and higher–order perturbations of travel time in isotropic and anisotropic media. *Stud. geophys. geod.*, **46**, 213–248, online at "http://sw3d.cz".

Klimeš, L. (2006): Common–ray tracing and dynamic ray tracing for S waves in a smooth elastic anisotropic medium. *Stud. geophys. geod.*, **50**, 449–461.

Klimeš, L. (2007): Coupling ray series. In: *Seismic Waves in Complex 3–D Structures, Report 17*, pp. 99–109, Dep. Geophys., Charles Univ., Prague, online at "http://sw3d.cz".

Klimeš, L. (2010): Transformation of spatial and perturbation derivatives of travel time at a general interface between two general media. In: *Seismic Waves in Complex 3–D Structures, Report 20*, pp. 103–114, Dep. Geophys., Charles Univ., Prague, online at "http://sw3d.cz".

Klimeš, L. & Bulant, P. (2004): Errors due to the common ray approximations of the coupling ray theory. *Stud. geophys. geod.*, **48**, 117–142.

Klimeš, L. & Bulant, P. (2006): Errors due to the anisotropic–common–ray approximation of the coupling ray theory. *Stud. geophys. geod.*, **50**, 463–477.

Pšenčík, I. (1998): Package ANRAY, version 4.10. In: *Seismic Waves in Complex 3–D Structures, Report 7*, pp. 403–404, Dep. Geophys., Charles Univ., Prague, online at "http://sw3d.cz".

Pšenčík, I. & Dellinger, J. (2001): Quasi–shear waves in inhomogeneous weakly anisotropic media by the quasi–isotropic approach: A model study. *Geophysics*, **66**, 308–319.

Pšenčík, I. & Farra, V. (2005): First–order ray tracing for qP waves in inhomogeneous, weakly anisotropic media. *Geophysics*, **70**, D65–D75.

Pšenčík, I. & Farra, V. (2007): First–order P–wave ray synthetic seismograms in inhomogeneous weakly anisotropic media. *Geophys. J. int.*, **170**, 1243–1252.

Pšenčík, I., Farra, V. & Tessmer, E. (2011): Comparison of the FORT approximation of the coupling ray theory with the Fourier pseudospectral method. In: *Seismic Waves in Complex 3–D Structures, Report 21*, pp. 129–165, Dep. Geophys., Charles Univ., Prague, online at "http://sw3d.cz".

Pšenčík, I., Farra, V. & Tessmer, E. (2012): Comparison of the FORT approximation of the coupling ray theory with the Fourier pseudospectral method. *Stud. geophys. geod.*, **56**, 35–64.

Thomson, C.J., Kendall, J-M. & Guest, W.S. (1992): Geometrical theory of shear–wave splitting: corrections to ray theory for interference in isotropic/anisotropic transitions. *Geophys. J. int.*, **108**, 339–363.